CrossMark

Ferromagnetism in Cu^{2+} doped ZnO nanoparticles and their physical properties

Pallavi G. Undre[1,2] · Prashant B. Kharat[1] · R. V. Kathare[2] · K. M. Jadhav[1]

Abstract

Cu^{2+} doped ZnO nanoparticles designated as Zn$_{1-x}$Cu$_x$O (x = 0.00, 0.02, 0.04, 0.06, 0.08 and 0.10) were prepared by sol–gel auto combustion technique. The modifications in structure, morphology, band gap, electrical, dielectric and magnetic properties due to Cu^{2+} doping were investigated through XRD, FE-SEM/EDAX, TEM/SAED, Raman, FT-IR, UV–Vis and VSM respectively. The analysis of XRD pattern reveals the incorporation of the dopants Cu^{2+} into ZnO lattice. The XRD spectra show that all the synthesized nanoparticles are a single crystalline phase with hexagonal wurtzite structure. The analysis of FE-SEM indicates that Cu^{2+} doping affects the surface morphology of ZnO. The compositional study performed by EDAX confirmed the presence of Zn, O, and Cu in stoichiometric proportion. TEM micrographs show the spherical shape of nanocrystals with small agglomeration. SAED patterns confirm the crystalline nature with hexagonal wurtzite structure. Raman spectra show the strongest peak at 437 cm^{-1} related to vibration of oxygen atoms in ZnO and also confirms optical phonon modes. FTIR result confirms the successful accompanying of Cu^{2+} ions into ZnO crystal lattice without changing its original structure. From DC electrical resistivity measurements it was found that electrical resistivity enhanced with increase in Cu^{2+} content. The measured dielectric parameters decreased with increase in Cu^{2+} content. An optical study revealed that the energy band gap decreased with doping of Cu^{2+} ions into ZnO nanoparticles. The VSM analysis shows the transformation of paramagnetic to superparamagnetic and superparamgnetic to ferromagnetic at room temperature due to Cu^{2+} doping in ZnO nanoparticles. The enhanced physical properties revealed that the prepared Cu^{2+} doped ZnO nanoparticles are the potential candidate for high-frequency devices, optoelectronic devices and spintronics devices application.

1 Introduction

Synthesis of nanomaterials is an interesting research topic for enhancing the nano-size, chemical compositions and their physical properties in the area of nanotechnology. There are conventional synthesis methods known from the times of 'Michael Faraday' for fabrication of nanoparticles. The various synthesis methods are developed for metal oxide nanoparticles. The synthesis methods are having the amount of modification and improvements on synthesis parameters that gives better control of particle size [1–3]. Metal oxide nanoparticles like CuO$_2$, SuO$_2$, TiO$_2$, ZnO etc.

a large number of applications in the field of storage devices, spintronic devices, gas sensors, photocatalyst, capacitor, etc. [4–11].

ZnO is a most promising II–IV group semiconductor with a direct wide band gap (3.37 eV) and have high exciton binding energy (60 MeV) for the optoelectronics device application. Doping is mostly used method for improvement of electrical, optical and magnetic properties of semiconductor materials. The doping of transition metals such as Co, Ni, Mn, Fe, Cu, etc. increases the surface area and also reduces the particle size of ZnO nanoparticles [12–15]. Doping of transition metal such as Cu^{2+} into ZnO which facilitate the construction of many electronic, optoelectronic, photodetection and spintronics devices [16–18].

Recently, optoelectronics properties of Cu doped ZnO nanoparticles were studied by sol–gel method and their frequency relaxation phenomenon [19]. Cu doped ZnO photocatalysts by co-precipitation method was investigated for removal of arsenic from drinking water by photocatalytic oxidation [20]. The Cu^{2+} doped ZnO nanoparticles sheets

✉ K. M. Jadhav
drjadhavkm@gmail.com

1   Department of Physics, Dr. Babasaheb Ambedkar Marathwada University, Aurangabad, MS, India

2   Department of Physics, Karmaveer Mamasaheb Jagdale Mahavidyalaya, Washi, Osmanabad, MS, India

synthesized by solution route in which PL measurements show tunable violet and yellow emissions used for the white-light-emitting devices and bio-imaging applications [21]. Cu doped ZnO synthesized by hydrothermal method, the magnetic results shows the ferromagnetism in Cu doped ZnO due to oxygen vacancies [22]. Another report on Cu^{2+} doped ZnO shows good crystal surface, good crystalline structure, better optical properties which can be appreciable for the fabrication of nano-optoelectronic devices [23]. Another report shows that Cu^{2+} doped ZnO nanoparticles in the presence of capping agents CTAB (cetyltrimethylammonium bromide) and SHMP (sodium hexametaphosphate), a blue shift of UV–Vis absorption spectra. SHMP is effective for controlling particle size and morphology of the particles [24]. The literature survey reveals that the Cu^{2+} doped ZnO nanoparticles is an interesting material for various applications.

The different physical and chemical synthesis approaches were developed to fabricate nano-dimensional ZnO, like solid-state reaction, co-precipitation, hydrothermal, sol–gel techniques, etc [25–32]. Among these techniques, sol–gel auto combustion technique is one of the most desirable, simple, cost-effective, controllability of composition and also suitable for large-scale production of nanomaterials [33, 34].

Though there are few of articles on Cu^{2+} doped ZnO semiconductor, the experimental results on structural, optical, electric, dielectric and magnetic properties show variation. Also, the doping level of Cu is not tested to its solubility limit. Therefore, the present work aims to synthesize Cu^{2+} doped ZnO nanoparticles with different concentration to its solubility limit by sol–gel auto combustion technique and to investigate the effect of Cu^{2+} doping on structural, microstructural, electric, dielectric, optical and magnetic properties of ZnO nanoparticles.

2 Experimental

2.1 Preparation of $Zn_{1-x}Cu_xO$ (x = 0.00, 0.02, 0.04, 0.06, 0.08 and 0.10) nanoparticles

$Zn_{1-x}Cu_xO$ (x = 0.00–0.10 with step size of 0.02) nanoparticles were prepared by sol–gel auto combustion technique. The citric acid was used as fuel and the metal nitrates to fuel ratio were taken as 1:1 according to propellant chemistry. All the chemicals used for the synthesis were of analytical grade purity, acquires from Sigma Aldrich and Merck. The appropriate proportion of zinc nitrate hexahydrate (Zn$(NO_3)_2$·$6H_2O$), copper nitrate trihydrate (Cu$(NO_3)_2$·$3H_2O$) and citric acid monohydrate ($C_6H_8O_7$·H_2O) were used. Firstly, nitrate solution prepared by an appropriate amount of zinc nitrate and copper nitrate was dissolved in 100 ml distilled water under constant stirring using magnetic stirrer.

Then citric acid was added to the nitrate solution. The solution was maintained at room temperature under constant stirring for ~ 1 h for a homogeneous solution. The prepared homogeneous solution was kept 90 °C on a hot plate for 3 h under constant stirring. Then the 'sol' get converted into 'gel' forms ensure that the complete reaction should be done. The 'gel' was next swelling into foam like and undergoes the strong self-propagating auto combustion reaction, it gives the fine powder. The prepared powders were grounded in 'pestle' and 'mortar'. Finally, collected powders were sintered using muffle furnace at 600 °C for 5 h. For further characterization studies the few gm annealed powder is pelletized using hydraulic press by applying a pressure 5 ton/cm^2. The chemical reaction of $Zn_{1-x}Cu_xO$ (x = 0.00, 0.02, 0.04, 0.06, 0.08 and 0.10) nanoparticles and systematic flow chart of synthesis technique with photographic presentations are shown in Fig. 1.

2.2 Characterization

The structural analysis of $Zn_{1-x}Cu_xO$ (x = 0.00–0.10) nanoparticles was carried out by X-ray diffraction technique (XRD) with Cu K_α radiation at 40 kV and 30 mA from 20°–80° (XRD, Bruker D8 Advance). The surface morphology of the $Zn_{1-x}Cu_xO$ (x = 0.00, 0.04, 0.10) nanoparticles was observed using field emission scanning electron microscopy (FESEM, JEOL JSM-6360). The composition of Zn, O, and Cu were examined by energy dispersive spectrometer using K and L line by energy dispersive spectroscopy (EDAX). The crystalline characteristic studied by transmission electron microscopy (TEM) and SAED pattern by 200 KV TECNAI G^2 20 microscope. The functional group and structural changes during the combustion reaction of $Zn_{1-x}Cu_xO$ (x = 0.00 and 0.10) nanoparticles were studied using Fourier transformer infra-red spectroscopy (FTIR) recorded in the range of 400–4000 cm^{-1} (FTIR, Perkin Elmer, Spectrum). Optical phonon modes and Raman active modes were recorded using Raman spectra of $Zn_{1-x}Cu_xO$ (x = 0.00 and 0.10) nanoparticles in the range of 300–800 cm^{-1} (Raman spectroscopy, Renishaw). Optical properties $Zn_{1-x}Cu_xO$ (x = 0.00, 0.02, 0.04, 0.06, 0.08 and 0.10) nanoparticles were studied using UV–Vis spectroscopy in the wavelength range 300–700 nm (Shimadzu Europa 1800). An electrical property such as DC electrical resistivity was carried out by a standard two-probe technique in the temperature range 300–550 K. The dielectric studies as dielectric constant, dielectric loss and dielectric loss tangent using LCR-Q meter (HIOKI-3532-500) in the frequency range 50 Hz–5 MHz. The sample used for the Raman spectroscopy, DC electrical resistivity and dielectric studies is in the form of pellets. Field dependent magnetization studies were carried out by vibrating sample magnetometer (VSM) at room temperature.
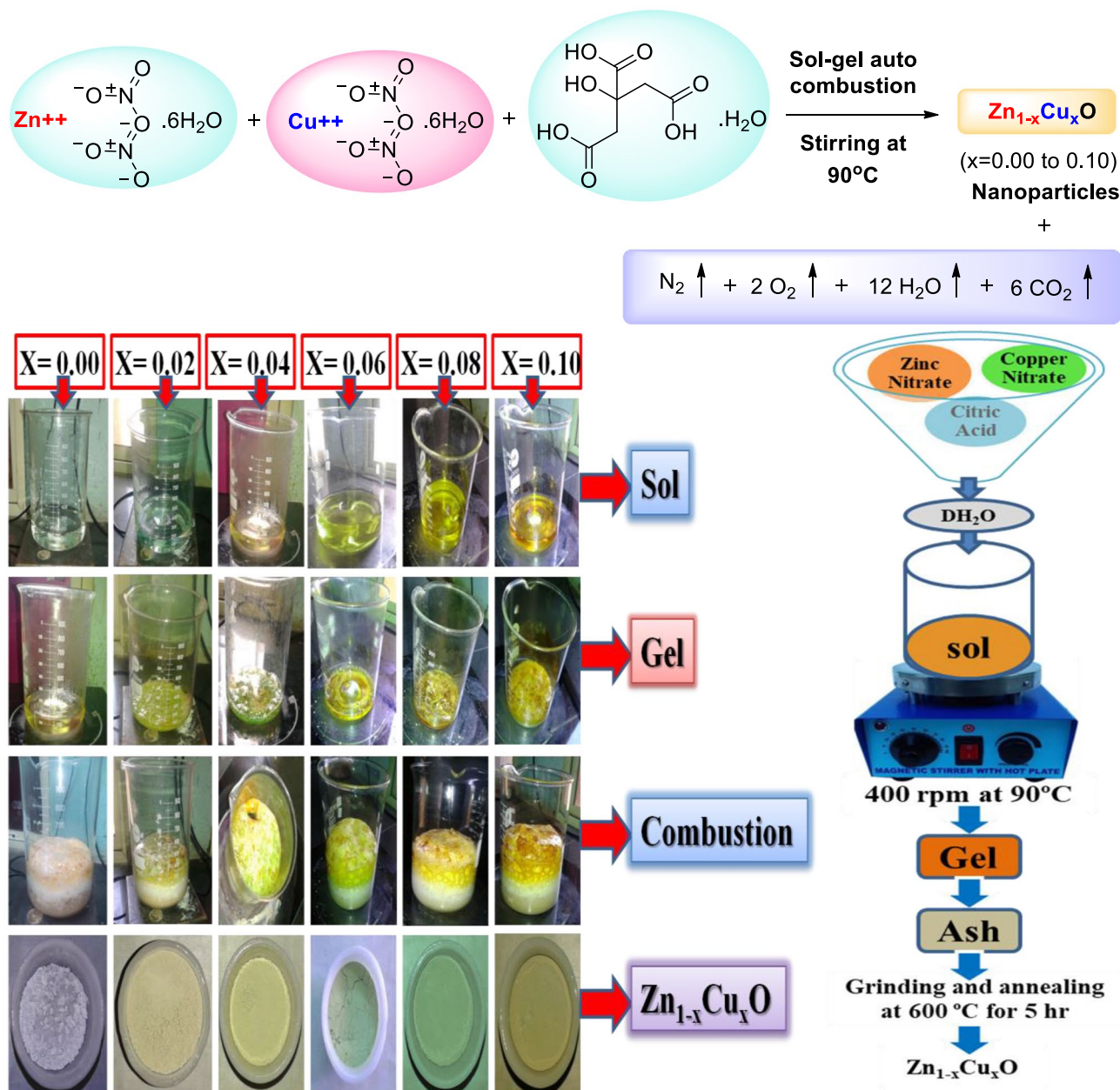
Fig. 1 Chemical reaction, photographic presentation and systematic flow chart of sol–gel auto combustion synthesis of $Zn_{1-x}Cu_xO$ (x = 0.00, 0.02, 0.04, 0.06, 0.08 and 0.10) nanoparticles

3 Results and discussions

3.1 XRD

The X-ray diffraction patterns of $Zn_{1-x}Cu_xO$ (x = 0.00, 0.02, 0.04, 0.06, 0.08 and 0.10) nanoparticles are shown in Fig. 2. The X-ray diffraction peaks clearly shows hexagonal wurtzite structure corresponding to the diffraction angles with planes 31.75° (100), 34.41° (002), 36.24° (101), 47.51° (102), 56.63° (110), 62.92° (103), 66.42° (200), 68.93°

(112), 69.11° (201) and 77.03° (004). The XRD spectra along the (101) plane show the variation of peak position and peak intensity by Cu^{2+} doping as compare to all peaks. The standard diffraction peaks of ZnO are nanocrystalline which belongs to the space group $P6_3mc$ and well matches with standard JCPDS card no. 36-1451 [35, 36]. From the XRD peaks, we can observe that peak intensity increases and also the full width at half maximum (FWHM) becomes wider with Cu^{2+} doping. This indicates that crystallinity is enhanced by Cu^{2+} doping into ZnO nanoparticles. Also,
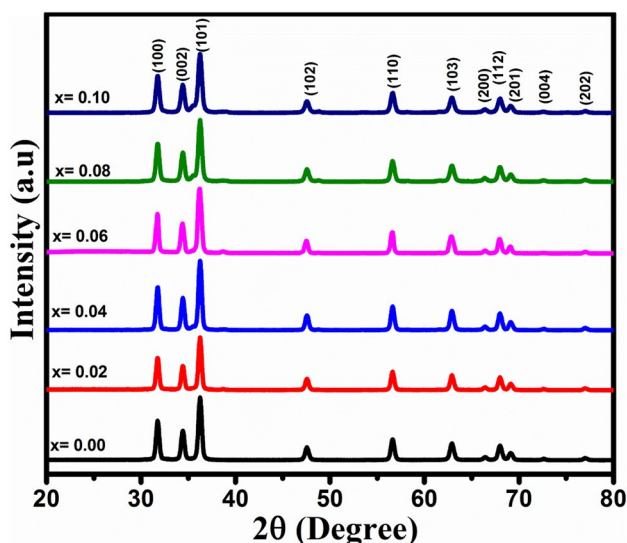
Fig. 2 The XRD patterns of $Zn_{1-x}Cu_xO$ nanoparticles

the Cu^{2+} ions are successfully occupied Zn^{2+} site without changing its original hexagonal wurtzite crystal structure [19]. The ionic radii of Cu^{2+} (0.73 Å) are very much closer to corresponding Zn^{2+} (0.74 Å). Therefore Cu can easily accompanying into Zn site into ZnO crystal lattice [37]. The Cu^{2+} ions are easily incorporated in ZnO lattice with solubility limit up to 10% without impurity phase shown in Fig. 2.

The average crystallite size (D) of the pure and Cu^{2+} doped ZnO nanoparticles are calculated from X-ray line broadening diffraction peaks of (101) plane using Debye Scherrer's Eq. (1) [38, 39].

$$D = \frac{0.9\lambda}{\beta \cos\theta} \tag{1}$$

where λ (1.5405 Å) is the wavelength of X-ray, β is full width at half maximum of the angular peak in radian along (101) plane and θ is Bragg's diffraction angle. Table 1 clearly shows the average crystallite size is reduced from ~ 21 to ~ 18 nm by the doping of Cu^{2+} content, which indicate that the prepared samples are nanocrystalline. The decrease of average crystallite size is mostly due to the distortion in the host ZnO lattice through the foreign impurity as Cu^{2+} ions.

This takes place decrease nucleation as well as subsequent growth rate by the doping of Cu^{2+} ions. A similar result of Cu^{2+} doping ZnO nanostructure within limit around x = 0.10 without impurity phase was also reported [38]. The lattice distortion of ZnO by Cu^{2+} doping enhances the strain moderately [40]. Further decrease in crystallinity, it gives the increasing nature of micro-strain by doping of Cu^{2+} ions. The micro-strain (ε) can be calculated using the Eq. (2) [41].

$$\varepsilon = \frac{\beta \cos\theta}{4} \tag{2}$$

Table 1 shows that as the doping of Cu^{2+} ions increases into ZnO lattice, the micro-strain (ε) also increases. Addition of Cu^{2+} the intrinsic stress is monotonically changed due to the changes in microstructure size and shape of the particles. So, it indicates that the increase in strain causes the increase in lattice constant by doping of Cu^{2+} ions into ZnO nanoparticles. For hexagonal nanostructure, the lattice constants 'a' and 'c' are calculated using the Eq. (3) [42].

$$\frac{1}{d^2} = \left[\frac{4}{3} \left(\frac{(h^2 + hk + k)^2}{a^2} + \frac{l^2}{c^2} \right) \right] \tag{3}$$

where, d is lattice spacing, (h, k, l) are Miller indices, 'a' and 'c' are lattice parameters. By the doping of Cu^{2+} ions as an alternative of Zn ions, their lattice sites increases which increases lattice constants 'a' and 'c'. The similar increasing trend of lattice constants is reported in the literature [23]. Table 1 shows the lattice parameters of Cu^{2+} doped ZnO is slightly greater than the pure ZnO due to the inequality of ionic radii Cu^{2+} (0.73 Å) and Zn^{2+} (0.74 Å). It observed that a systematic variation in lattice parameter. Also, the c/a ratio is a good match with ideally close-packed hexagonal structure, i.e. 1.633 shown in Table 1. The result clearly illustrates that there is no change in hexagonal wurtzite structure of ZnO after doping of Cu^{2+}. The volume of the unit cell for hexagonal crystal structure has been calculated using Eq. (4) [43].

$$V = 0.866 a^2 c \tag{4}$$

The volume of the unit cell is directly related to the lattice parameter 'a' and 'c' shows the similar behavior tabulated

Table 1 Lattice parameters, c/a ratio, crystallite size, volume, micro-strain, positional parameter and bond length of $Zn_{1-x}Cu_xO$ (x = 0.00, 0.02, 0.04, 0.06, 0.08 and 0.10) nanoparticles

'x'	Lattice parameter		c/a	D (nm)	V (Å)³	ε × 10⁻³	u	L (Å)
	a (Å)	c (Å)						
0	3.2506	5.2039	1.6009	21.86	47.618	1.620	0.3800	1.978
0.02	3.2518	5.2147	1.6036	21.12	47.752	1.660	0.3794	1.979
0.04	3.2529	5.2156	1.6033	20.23	47.793	1.690	0.3796	1.980
0.06	3.2537	5.2161	1.6031	19.25	47.821	1.770	0.3797	1.981
0.08	3.2549	5.2169	1.6028	18.34	47.864	1.810	0.3798	1.981
0.1	3.2457	5.2176	1.6075	18.15	47.894	1.880	0.3799	1.982

in Table 1. Bond length is also related to lattice parameters have been calculated using Eq. (5) [44].

$$L = \sqrt{\left(\sqrt{(\frac{a^2}{3} + \left(\frac{1}{2} - u\right)^2 c^2)} \right)} \qquad (5)$$

where u is oxygen parameter of hexagonal structure, i.e. $u = {a^2}/{3c^2} + 0.25$. The bond length of pure and Cu^{2+} doped ZnO nanoparticles given in Table 1. It is observed that bond length increases with increase in Cu^{2+} ions [45]. These parameters evidence that prepare $Zn_{1-x}Cu_xO$ (x = 0.00, 0.02, 0.04, 0.06, 0.08 and 0.10) nanoparticles have good crystallinity. While a decrease in crystallinity was observed in distortion in the host ZnO lattice due to Cu^{2+} doping.

3.2 FE-SEM/EDAX

The surface morphology and information regarding the growth mechanism of $Zn_{1-x}Cu_xO$ (x = 0.00. 0.04 and 0.10) nanoparticles was examined by promising field emission scanning electron microscopy (FE-SEM) technique. The FE-SEM images of present nanoparticles show a group of bright and dark regions shown in Fig. 3 with the resolution taken as 500 nm. Figure 3 reveals that the grain size of the present nanoparticles is in order of nanometer range. The prepared nanoparticles show the formation of homogeneous, uniform distribution, good connectivity and spherical morphology. It also seemed that irregular grain distribution and a large number of agglomeration is there in present nanoparticles. After the doping of Cu^{2+} in ZnO nanoparticles, the small particles are loosely agglomerated. The grain size of present samples determined by FE-SEM images is shown in Table 2. It is observed that the average grain size decreases with an increase in Cu^{2+} doping in ZnO lattice. The doping of Cu^{2+} ions strongly influences the grain size as well as the morphology of ZnO nanoparticles. This result is correlated to XRD results. The specific surface area was calculated by using Eq. (6).

$$S = \frac{6000}{\rho_x D}\% \qquad (6)$$

where ρ_x is the X-ray density, D is average grain size. According to the specific surface area, the surface activity

can be changed in the same material with the same weight and volume. The calculated specific surface area is tabulated in Table 2. The specific surface area is increased with a decrease in grain size. The surface area to volume ratio was also calculated and values are tabulated in Table 2. The energy dispersive spectroscopy (EDAX) of pure and Cu^{2+} doped ZnO nanoparticles are done for knowing the information related to purity and presence of Cu^{2+} ions in ZnO lattice. The energy dispersive spectroscopy (EDAX) technique confirms the stoichiometric presence of Zn, O and Cu into prepared nanoparticles. The weight percentage of elements is tabulated in Table 2. Figure 3 clearly indicates that the intensity of Cu^{2+} ions increasing with the Cu^{2+} concentration in ZnO lattice. EDAX analysis indicates that the successful doping of Cu^{2+} ions in ZnO nanoparticles.

3.3 TEM/SAED

The transmission electron microscopy (TEM) with the selected area electron diffraction (SAED) patterns is a principal technique for getting atomic structure of solid crystal and information regarding the crystalline nature of nanoparticles. Figure 4 shows the magnified TEM images with SAED patterns of $Zn_{1-x}Cu_xO$ (x = 0.00 and 0.10) nanoparticles. From Fig. 4 TEM micrographs shows the shape of prepared nanoparticles is nearly spherical with small aggregation. However, there is some slight degradation in the crystallinity of Cu^{2+} doped ZnO nanoparticles which is supported by SAED pattern. In SAED pattern clear bright spots can be indicated as the crystalline hexagonal structure of ZnO. Analysis of these SAED patterns indicates that besides the diffraction rings of the wurtzite structure of ZnO, there were no additional rings observed. The TEM micrographs and SAED patterns evidence that the prepared nanoparticles are single crystalline phase having hexagonal wurtzite crystal structure, no evident change on lattice orientation. The concentric rings by SAED patterns that match with standard wurtzite structure of ZnO [46].

3.4 Raman spectroscopy

Raman spectroscopy of $Zn_{1-x}Cu_xO$ (x = 0.00 and 0.10) nanoparticles at the room temperature in the range of 400–800 cm^{-1} shown in Fig. 5. The technique is mostly

Table 2 Average grain size, specific surface area, surface to volume ratio, weight (%) of elements and activation energy of $Zn_{1-x}Cu_xO$ (x = 0.00, 0.04 and 0.10) nanoparticles

| Conc. x	Average grain size (nm)	Specific surface area (cm²/g)	S/V ratio	Weight percentage of the elements (at.%)			Activation energy (eV)
				Zn^{2+}	Ni^{2+}	O^{2+}	
0.00	48.41	22.13	0.464	50	–	50	0.71
0.04	45.3	23.65	0.494	21.62	35.13	43.25	0.76
0.10	43.08	24.87	0.519	15.43	41.98	42.59	0.85
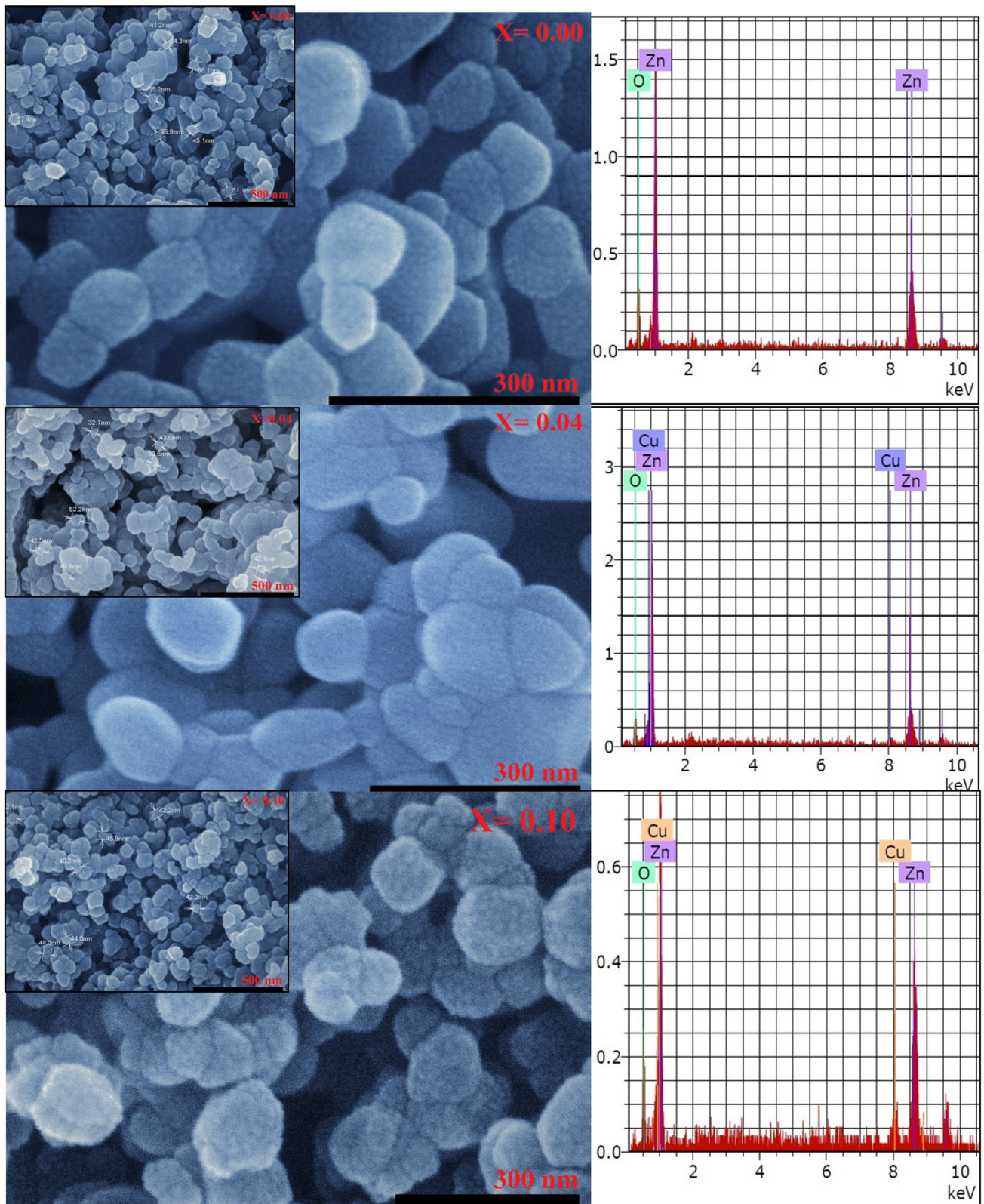
**Fig. 3** FE-SEM images and EDAX spectra of $Zn_{1-x}Cu_xO$ (x = 0.00, 0.04 and 0.10) nanoparticles
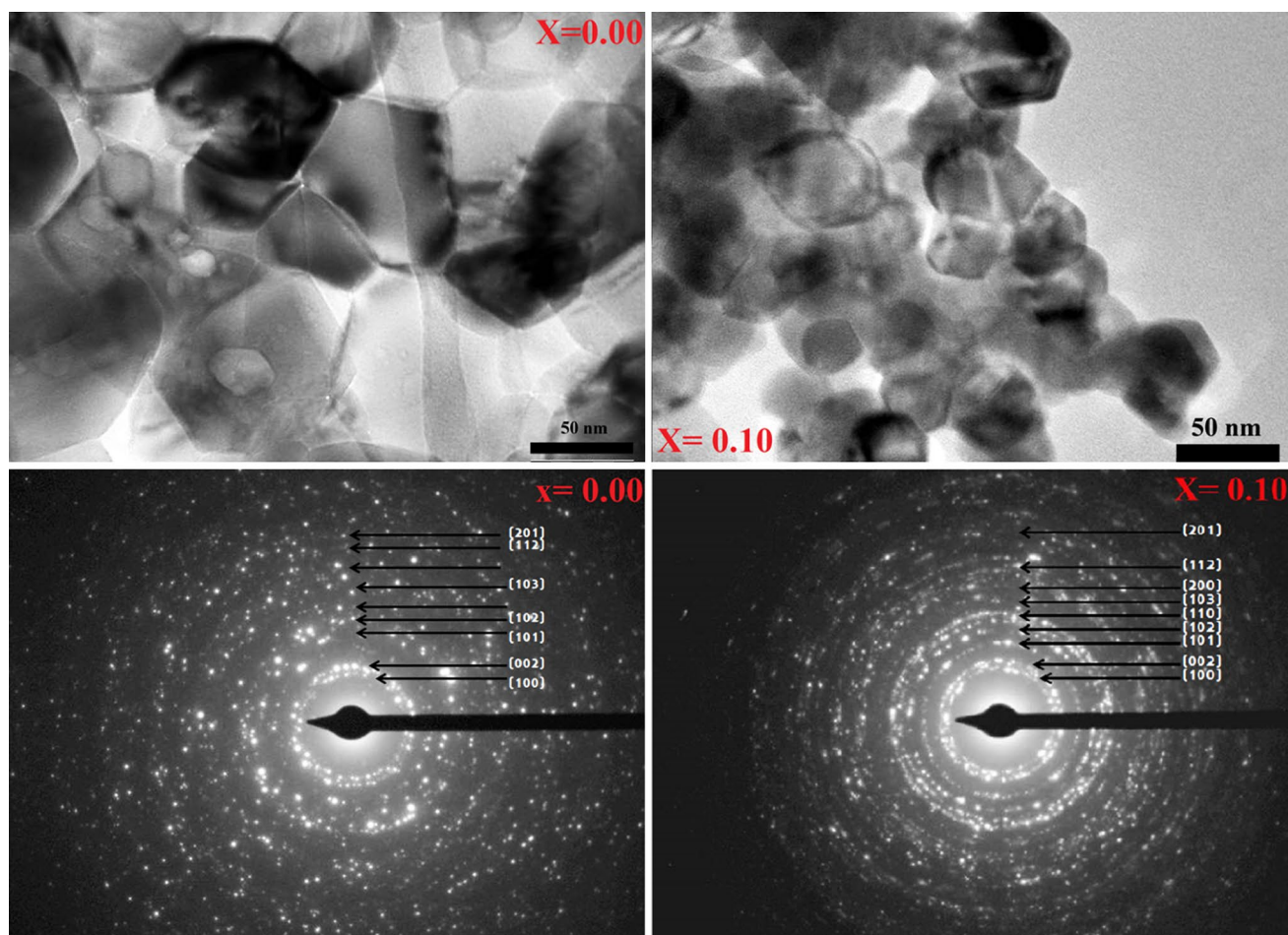
Fig. 4 TEM images and SAED patterns of $Zn_{1-x}Cu_xO$ (X = 0.00 and 0.10) nanoparticles

used to study the quality of nanoparticles, phase purity for understanding the transport properties and also detect the interaction of optical phonon modes with free carriers [47]. From Fig. 5 the sharp peak at 437 cm^{-1} is attributed to ZnO high-frequency optical phonon mode E_2 (high). E_2 (high) mode is a non-polar mode which associated with the variation of oxygen and ZnO sub-lattice respectively. This characteristics peak confirms the formation of single crystalline phase hexagonal wurtzite structure of prepared nanoparticles. Also, it does not change its original structure by doping of Cu^{2+}. Figure 5 observed that the E_2 (high) mode shift from ~437 to 438 cm^{-1} and also decrease in peak intensity. The slightly shifting of the E_2 (high) mode indicates that Cu^{2+} doping produces lattice distortion in ZnO crystal lattice. There is another peak at ~610 cm^{-1} is assigned to E_1 (low) mode, this polar mode is related to the oxygen vacancies. There are no another modes found in the spectra. The Raman analysis confirms the successful accompanying of Cu^{2+} ions into ZnO lattice.
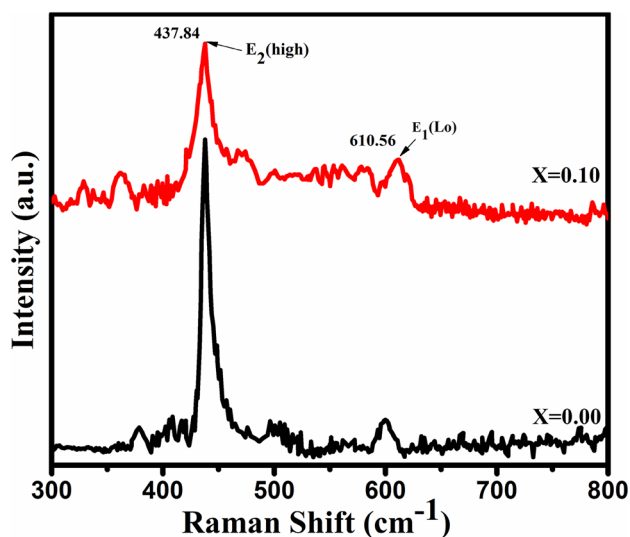
Fig. 5 Raman spectra of $Zn_{1-x}Cu_xO$ (X = 0.00 and 0.10) nanoparticles
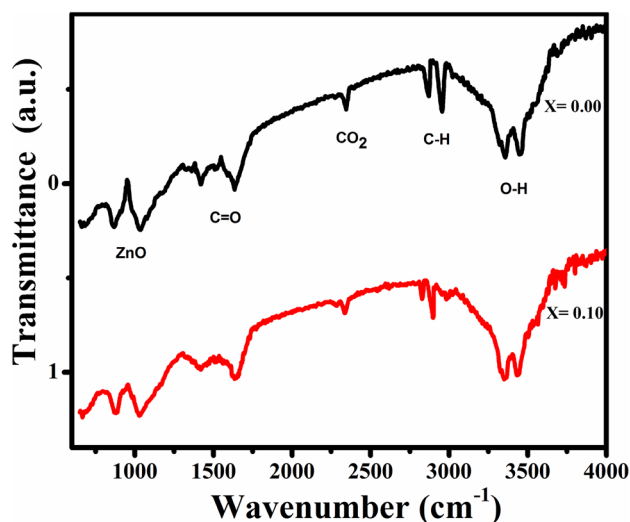
Fig. 6 Fourier transformation infra-red spectra (FTIR) of $Zn_{1-x}Cu_xO$ (X = 0.00 and 0.10) nanoparticles

3.5 FTIR

Figure 6 shows the Fourier transformation infrared spectra (FTIR) of $Zn_{1-x}Cu_xO$ (x = 0.00 and 0.10) nanoparticles recorded at the range of 500–4000 cm^{-1}. The FTIR spectra were used to get the information about the chemical bonding, elemental constituents, vibrational frequencies and also the stretching modes in the nanoparticles. The extensive observation peak around the ~ 3456 cm^{-1} to ~ 3349 cm^{-1} are recognized to O–H stretching vibration in Cu–ZnO lattice of H_2O [48]. The weak absorption peaks found at ~ 2800 to ~ 2950 cm^{-1} are the symmetric and asymmetric nature of C–H stretching mode. The absorption peak signed between ~ 2280 and ~ 2340 cm^{-1} is due to the CO_2 molecule existence in the air. The sharp peaks observed at 1300 to ~ 1600 cm^{-1} are attributed to the bonding of H–O–H is the physisorption of H_2O.

Moreover, the slight shifting of the absorption peak position was observed by doping of Cu^{2+} into ZnO lattice. The vibrational bands observed at ~ 750 cm^{-1} to ~ 1100 cm^{-1} are related to the ZnO stretching frequencies bands [49]. This can be recognized as the fundamental transverse optical phonon mode. According to the theory of vibrational modes in the mixed crystal structure, the doping concentration results are in an upward shifting. From these results, it reveals that successful doping of Cu^{2+} into ZnO lattice.

3.6 DC electrical resistivity

DC electrical resistivity at room temperature is associated with zinc interstitials and oxygen vacancy, i.e. intrinsic defect, which can be lead to the shallow donor of ZnO [45]. The DC electrical resistivity was measured in the

temperature range 300–550 K. The electrical resistivity (ρ) was estimated from the Eq. (7) [46].

$$\rho = \frac{VA}{It} \tag{7}$$

where V is the applied voltage, A is the area of the pelletized samples, I is the measured current and t is the thickness of pellet. The plots of electrical resistivity versus temperature are shown in Fig. 7. The electrical resistivity was observed to increase with the increase in Cu^{2+} doping into ZnO nanoparticles. The overall trend of pure and Cu^{2+} doped ZnO nanoparticles shows a decrease in electrical resistivity with respective temperature. The doping of Cu^{2+} ions into ZnO lattice can be simply ionized due to the small difference in ionization potential of Cu^{2+} ions, it increases the donor concentration than the subsequent increase in electrical resistivity. The doping of metal ions, i.e., Cu^{2+} might create a charge carrier like electron or holes as well as create oxygen vacancies. These oxygen vacancies can act as an active medium for charge carriers so that the electrical conductivity values increase significantly. Also, the temperature dependence on the DC electrical resistivity by Arrhenius equation [46]. The Arrhenius equation is given by (8).

$$\rho = \rho_0 \exp\left(\frac{E_a}{k_B T}\right) \tag{8}$$

whereas ρ_0 is a pre-exponential factor, E_a as activation energy, k_B as Boltzmann constant and T is the temperature in Kelvin. Figure 7 inset shows the Arrhenius plots of $Zn_{1-x}Cu_xO$ (x = 0.00, 0.02, 0.04, 0.06, 0.08 and 0.10) nanoparticles i.e. log ρ versus 1000/T. The activation energy E_a was estimated by using the slope of each composition, which
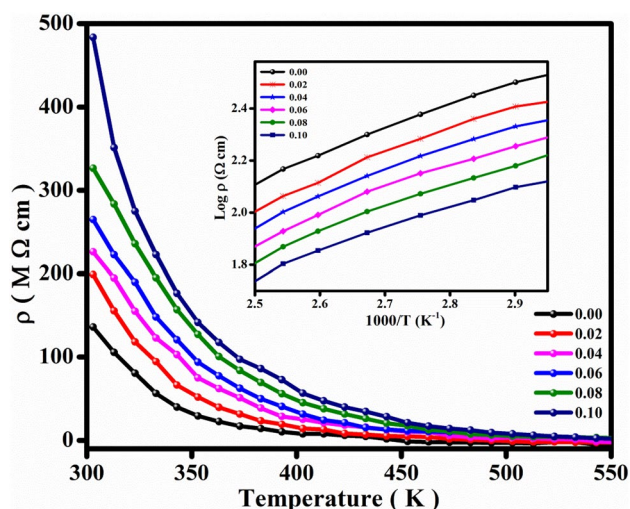
Fig. 7 The typical plots of electrical resistivity versus temperature of $Zn_{1-x}Cu_xO$ (x = 0.00 0.02, 0.04, 0.06, 0.08 and 0.10) nanoparticles

has been found that activation energy increases by increasing Cu^{2+} doping into ZnO nanoparticles [19]. The activation energy was tabulated in Table 2. The electrical resistivity and activation energy were increased with increase in Cu^{2+} doping into ZnO nanoparticles, which shows the semiconducting nature.

3.7 Dielectric study

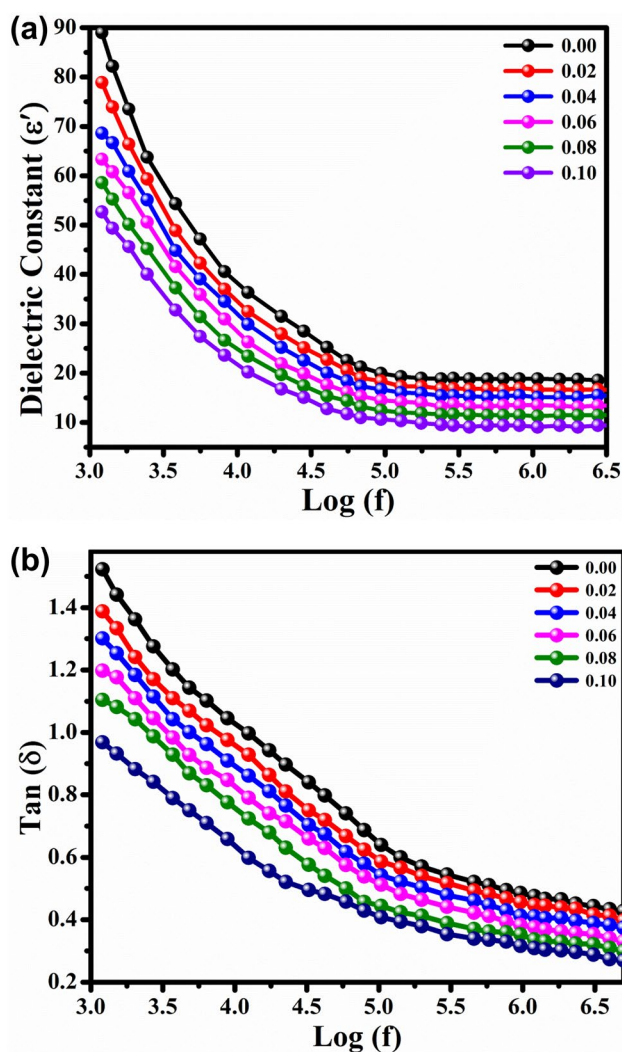The dielectric study of $Zn_{1-x}Cu_xO$ (x = 0.00–0.10) nanoparticles was carried out by LCR-Q meter with a corresponding frequency of applied electric field at room temperature. The dielectric studies of solid materials as a dielectric constant was estimated by Eq. (9) [50].

$$\varepsilon' = \frac{cd}{\varepsilon_0 A} \tag{9}$$

where c is capacitance, d is the thickness, ε_0 is the permittivity of free space and A is the cross-sectional area of the pellet. Variation of dielectric constant (ε') with the function of the frequency of pure and Cu^{2+} doped ZnO nanoparticles shown in Fig. 8a. It was observed that the maximum value of dielectric constant decreases with increase in frequency and reaches a constant at maximum frequency. The decreased value of dielectric constant has been caused by Cu^{2+} doping into ZnO due to the grain boundaries and oxygen vacancy in the ZnO lattice. The decreasing nature of dielectric constant may also attribute to the small dielectric polarizability of Cu^{2+} ions as comparing with Zn^{2+} ions. According to the Maxwell–Wagner model designed for the heterogeneous double structure [51]. From this model, there are two layers of the dielectric medium that one is more conductive and other is lower conducting. On which more conducting layer and lower conducting layer basically depends on grains and grain boundaries respectively. The dielectric loss (ε'') was calculated by Eq. (10) [50].

$$\varepsilon'' = \varepsilon' \tan \delta \tag{10}$$

where the energy loss was expressed by dielectric loss tangent (tan δ). The dielectric loss tangent is proportional to the energy loss from the applied field into the sample, which was a dielectric loss. From Fig. 8b shows the variation of dielectric loss tangent (tan δ) with frequency at the room temperature of $Zn_{1-x}Cu_xO$ (x = 0.00–0.10) nanoparticles. This observed curve shows the dielectric loss tangent (tan δ) decreases respectively with an increase in frequency. The doping of Cu^{2+} increases into ZnO nanoparticles, the dielectric constant with respective frequency decreases due to the space charge polarization. The space charge polarization decrease with increase in frequency and then reaches constant value due to the certain frequency of external field that hopping between different metal ions as Cu^{2+} and Zn^{2+} of Cu^{2+} doped ZnO nanoparticles. The decreasing behavior

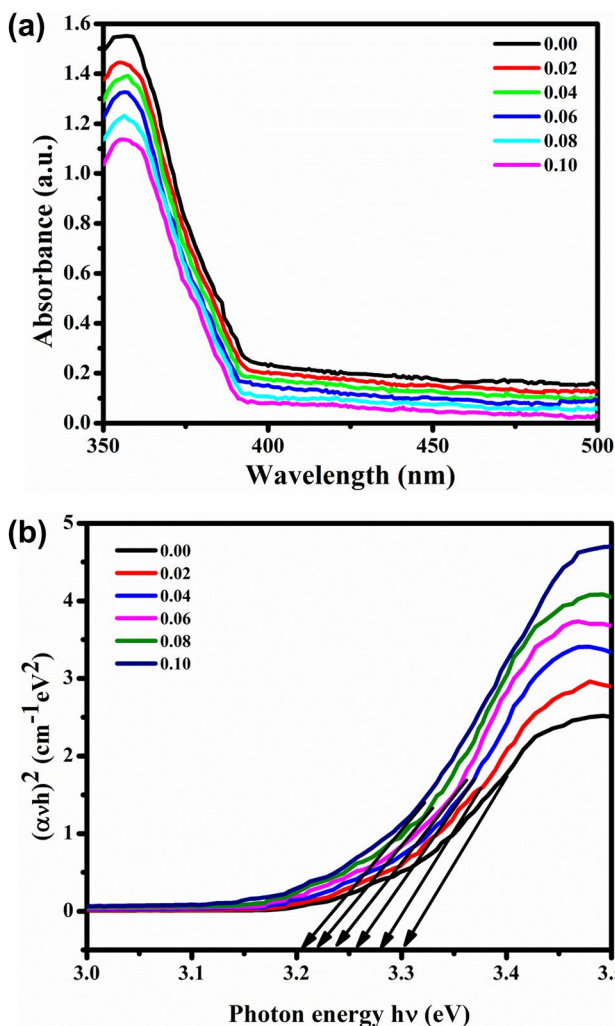**Fig. 8 a** Variation of dielectric constant (ε') with function of frequency of $Zn_{1-x}Cu_xO$ (x = 0.00, 0.02, 0.04, 0.06, 0.08 and 0.10) nanoparticles. **b** Variation of dielectric loss tangent (tan δ) with frequency of $Zn_{1-x}Cu_xO$ (x = 0.00, 0.02, 0.04, 0.06, 0.08 and 0.10) nanoparticles

of dielectric properties with frequency is natural because any species contributed to the polarizability is found lagging behind the applied field at higher frequencies [52].

3.8 Optical study

The optical absorption of the $Zn_{1-x}Cu_xO$ (x = 0.00–0.10) nanoparticles was studied by using UV–Vis spectra are shown in Fig. 9a. It can be observed that the strong band edge visible around 360 nm, which shows a red shift in the band edge due to interband transitions at the fundamental edge [37]. Also, the Cu^{2+} played an important role in the charge transfer transition that introduces a shallow number of energy levels inside air band, i.e. most famous
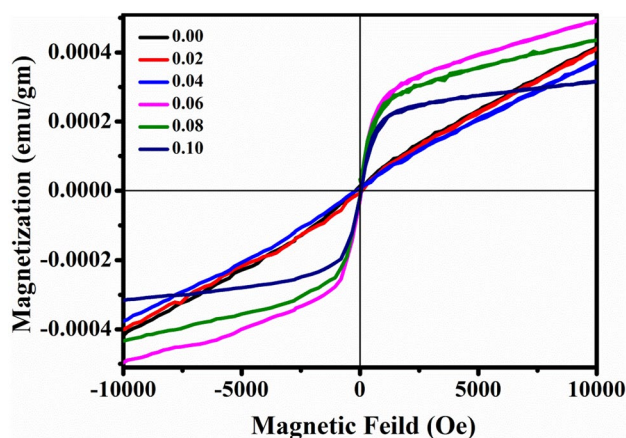
Fig. 10 M–H plots of $Zn_{1-x}Cu_xO$ (x = 0.00, 0.02, 0.04, 0.06, 0.08 and 0.10) nanoparticles

Fig. 9 a Optical absorption spectra of $Zn_{1-x}Cu_xO$ (x = 0.00, 0.02, 0.04, 0.06, 0.08 and 0.10) nanoparticles. **b** The $(\alpha h\nu)^2$ versus hν curves for the optical band gap determination of $Zn_{1-x}Cu_xO$ (x = 0.00, 0.02, 0.04, 0.06, 0.08 and 0.10) nanoparticles

Burstein–Moss effect [53]. It has been indicated that doping of Cu^{2+} ions into ZnO lattice. Figure 9a shows that the redshift in energy band gap with increasing Cu^{2+} doping by sp–d exchange interaction between ZnO band electrons and localized d-electron in Cu doping. The optical band gap energy of pure and Cu^{2+} doped ZnO nanoparticles are estimated by the Tauc's model. The energy band gap (E_a) is a most important role in semiconductors, which can figure out their application in optoelectronic devices [54]. The Tauc's relation is given by Eq. (11) [55].

$$ah\nu = A(h\nu - E_g)^n \tag{11}$$

whereas, α be the absorption coefficient, A is a band edge sharpness constant, h is Planck's constant, ν be the frequency of light radiation, E_g is the energy band gap and n = 1/2, i.e. direct allowed transition. The energy band gap (E_g) was

estimated by plotting $(\alpha h\nu)^2$ versus hν, plot to x-axis was extrapolating the linear portion. Figure 9b shows the variation of energy band gap of $Zn_{1-x}Cu_xO$ (x = 0.00–0.10) nanoparticles. Which is observed that (3.3–3.2 eV) energy band gap decreases with increase in Cu^{2+} doping into ZnO lattice [56]. This modification in the energy band gap by doping of Cu^{2+} into ZnO makes them suitable for a various application like optoelectronic devices.

3.9 Magnetic study

The magnetization studies were carried out at room temperature for $Zn_{1-x}Cu_xO$ (0.00–0.10 in step of 0.02) nanoparticles by VSM at varying applied magnetic field. The Fig. 10 clearly shows the paramagnetic behavior for pure ZnO nanoparticles at room temperature [57]. The paramagnetic nature is almost linear at normal temperature with regular field strength according to Langevin's theory. The paramagnetic behavior was observed when the presence of magnetic ions generated by an electric or magnetic field. The paramagnetic nature of pure ZnO was observed in our case where magnetic ions are not presented. This result was found due to the Zn vacancies were presented during the synthesis of ZnO nanoparticles. The interaction of Zn atoms is nearest to Zn vacancy with a 2p electron of oxygen atom [58]. Cu^{2+} doped ZnO nanoparticles with 0.02 and 0.04 concentration observed the superparamagnetic behavior at room temperature shown in Fig. 10. The absence of hysteresis loop at room temperature in a lower concentration of Cu^{2+} doped ZnO nanoparticles which shows the superparamagnetic behavior [59]. The Cu^{2+} doped ZnO nanoparticles with concentration as 0.06–0.10 shows room temperature ferromagnetic behavior shown in Fig. 10. The origin of ferromagnetism in transition metal as Cu^{2+} doped ZnO nanoparticles have various assumption like different intrinsic and extrinsic

defects [60, 61]. The extrinsic defect due to the secondary phase or impurity and intrinsic defects are such as zinc and oxygen vacancy. The ferromagnetic property of Cu^{2+} doped ZnO nanoparticles appearances due to the increased number of defects, oxygen vacancies and exchange interactions in between Cu^{2+} and O ions spin moment. The magnetic phase is changed paramagnetic to ferromagnetic due to delocalized carriers like holes and electrons (from valence band) and localized d spins on Cu^{2+} ions. Therefore the appearance of ferromagnetism due to the presence of free carriers and the free carriers induced by the Cu^{2+} doping into ZnO nanoparticles. The room temperature ferromagnetism is possible due to the presence of oxygen vacancies and Zn vacancies. The carrier mediated interaction between transition metal ions and free carriers also responsible for ferromagnetism [62]. The saturation magnetization values were varied with Cu^{2+} concentration in ZnO nanoparticles as 3.1×10^{-4} to 4.9×10^{-4} emu/g. These properties exhibit due to the extrinsic and intrinsic phenomenon. The extrinsic defect occurred due to secondary phases; by XRD result, secondary phase is not found. This property based on intrinsic defect occurred by zinc and oxygen vacancies and associated with magnetism. The transformation of paramagnetic to ferromagnetic phase observed may be due to the Cu^{2+} doping in ZnO nanoparticles. Also by the increased Cu^{2+} concentration, the ferromagnetic properties were enhanced [63].

4 Conclusion

The present work demonstrates the synthesis of $Zn_{1-x}Cu_xO$ (0.00–0.10 with a step of 0.02) nanoparticles via sol–gel auto combustion method. The successful doping of Cu^{2+} ions in ZnO nanoparticles with solubility limit 10% without impurity peaks confirmed by XRD. The variation of lattice parameters, crystalline size, volume, micro-strain and bond length shows the successful doping of Cu^{2+} ions into ZnO nanoparticles. FE-SEM/EDAX analysis reveals that prepared nanoparticles are in nano-crystalline in nature and most of the particles are spherical and agglomerated. Grain size is decreased by Cu^{2+} doping. The nanosized nature and crystallinity of Cu^{2+} doped ZnO nanoparticles confirmed by TEM and SAED pattern. The successful doping of Cu^{2+} in ZnO nanoparticles confirms by FTIR spectra. Raman spectra show optical phonon modes are present and it also confirms single phase crystal geometry of ZnO nanoparticles by Cu^{2+} doping. The DC electrical resistivity as well as activation energy is found to be increased by doping of Cu^{2+} in ZnO lattice. The dielectric constant and dielectric loss tangent was observed to decrease with the increase of Cu^{2+} doping into ZnO lattice as a function of frequency. The optical band gap energy decreases with increase Cu^{2+} doping. The magnetic study reveals the prepared nanoparticles have

a different magnetic phase like pure ZnO shows the paramagnetic nature due to the absence of an intrinsic defect, $Zn_{1-x}Cu_xO$ x ≥ 0.04 nanoparticles shows the superparamagnetic behavior and x = 0.06–0.10 nanoparticles shows the ferromagnetic behavior which is applicable for spintronics application point of view. The obtained results were found to be useful for fabrication of nano-optoelectronic, spintronics and high-frequency device applications.

Compliance with ethical standards

Conflict of interest The authors declare that they have no conflict of interest.

References

1. S.M. Hosseinpour-Mashkani, A. Sobhani-Nasab, M. Mehrzad, J. Mater. Sci. Mater. Electron. **27**, 5758–5763 (2016)
2. M. Rahimi-Nasrabadi, M. Behpour, A. Sobhani-Nasab, S.M. Hosseinpour-Mashkani, J. Mater. Sci. Mater. Electron. **26**, 9776–9781 (2015)
3. M. Rahimi-Nasrabadi, M. Behpour, A. Sobhani-Nasab, M.R. Jeddy, J. Mater. Sci. Mater. Electron. **27**, 11691–11697 (2016)
4. W. Lee, Y.S. Lim, S. Kim, J. Jung, Y.-K. Han, S. Yoon, L. Piao, S.-H. Kim, J. Mater. Chem. **21**, 6928–6933 (2011)
5. M.S. Park, G.X. Wang, Y.M. Kang, D. Wexler, S.X. Dou, H.K. Liu, Angew. Chem. **119**, 764–767 (2007)
6. A. Jaroenworaluck, W. Sunsaneeyametha, N. Kosachan, R. Stevens, Surf. Interface Anal. **38**, 473–477 (2006)
7. R. Saravanan, K. Santhi, N. Sivakumar, V. Narayanan, A. Stephen, Mater. Charact. **67**, 10–16 (2012)
8. A. Javidan, M. Ramezani, A. Sobhani-Nasab, S.M. Hosseinpour-Mashkani, J. Mater. Sci. Mater. Electron. **26**, 3813–3818 (2015)
9. M. Mansournia, S. Rafizadeh, S.M. Hosseinpour-Mashkani, Ceram. Int. **42**, 907–916 (2016)
10. C.B. Ong, L.Y. Ng, A.W. Mohammad, Renew. Sustain. Energy Rev. **81**, 536–551 (2018)
11. N.A. Hammed, A.A. Aziz, A.I. Usman, M. Qaeed, Ultrason. Sonochem. **50**, 172–181 (2019)
12. M. Arshad, A. Azam, A.S. Ahmed, S. Mollah, A.H. Naqvi, J Alloys Compd. **509**, 8378–8381 (2011)
13. S. Kant, A. Kumar, Adv. Mater. Lett. **3**, 350–354 (2012)
14. B. Straumal, B. Baretzky, A. Mazilkin, S. Protasova, A. Myatiev, Straumal P., J. Eur. Ceram. Soc. **29**, 1963–1970 (2009)
15. M.M. Hassan, W. Khan, A. Azam, A. Naqvi, J. Lumin. **145**, 160–166 (2014)
16. Z. Zhang, J.B. Yi, J. Ding, L.M. Wong, H.L. Seng, S.J. Wang, J.G. Tao, G.P. Li, G.Z. Xing, T.C. Sum, J. Phys. Chem. C **112**, 9579–9585 (2008)
17. N. Kouklin, Adv. Mater. **20**, 2190–2194 (2008)
18. B.K. Das, T. Das, K. Parashar, A. Thirumurugan, S. Parashar, J. Mater. Sci. Mater. Electron. **28**, 15127–15134 (2017)
19. K. Omri, A. Bettaibi, K. Khirouni, L. El Mir, Physica B **537**, 167–175 (2018)
20. V. Vaiano, G. Iervolino, L. Rizzo, Appl. Catal. B **238**, 471–479 (2018)
21. R.-C. Wang, H.-Y. Lin, Mater. Chem. Phys. **125**, 263–266 (2011)

22. M. Zhu, Z. Zhang, M. Zhong, M. Tariq, Y. Li, W. Li, H. Jin, K. Skotnicova, Y. Li, Ceram. Int. **43**, 3166–3170 (2017)

23. S. Muthukumaran, R. Gopalakrishnan, Opt. Mater. **34**, 1946–1953 (2012)

24. P. Dhamodharan, R. Gobi, N. Shanmugam, N. Kannadasan, R. Poonguzhali, S. Ramya, Spectrochim. Acta A **131**, 125–131 (2014)

25. Z.-P. Sun, L. Liu, L. Zhang, D.-Z. Jia, Nanotechnology **17**, 2266 (2006)

26. R. Kripal, A.K. Gupta, R.K. Srivastava, S.K. Mishra, Spectrochim. Acta A **79**, 1605–1612 (2011)

27. A.N.P. Madathil, K. Vanaja, M. Jayaraj, *Nanophotonic Materials IV* (International Society for Optics and Photonics, San Diego, 2007), p. 66390J

28. A.K. Zak, M.E. Abrishami, W.A. Majid, R. Yousefi, S. Hosseini, Ceram. Int. **37**, 393–398 (2011)

29. S.M. Hosseinpour-Mashkani, M. Ramezani, Mater. Lett. **130**, 259–262 (2014)

30. A. Sobhani-Nasab, M. Maddahfar, S.M. Hosseinpour-Mashkani, J. Mol. Liq. **216**, 1–5 (2016)

31. S.M. Hosseinpour-Mashkani, M. Maddahfar, A. Sobhani-Nasab, J. Mater. Sci. Mater. Electron. **27**, 474–480 (2016)

32. H. Mirzaei, M. Darroudi, Ceram. Int. **43**, 907–914 (2017)

33. M. Vafaee, M.S. Ghamsari, Mater. Lett. **61**, 3265–3268 (2007)

34. A. Sobhani-Nasab, A. Ziarati, M. Rahimi-Nasrabadi, M.R. Ganjali, A. Badiei, Res. Chem. Intermed. **43**, 6155–6165 (2017)

35. L. Shen, N. Bao, K. Yanagisawa, K. Domen, C.A. Grimes, A. Gupta, J. Phys. Chem. C **111**, 7280–7287 (2007)

36. D. Raoufi, J. Lumin. **134**, 213–219 (2013)

37. R. Elilarassi, P.S. Rao, G. Chandrasekaran, J. Sol-Gel Sci. Technol. **57**, 101–108 (2011)

38. K. Raja, P. Ramesh, D. Geetha, Spectrochim. Acta A **131**, 183–188 (2014)

39. A. Ziarati, A. Sobhani-Nasab, M. Rahimi-Nasrabadi, M.R. Ganjali, A. Badiei, J. Rare Earth **35**, 374–381 (2017)

40. L.-H. Ye, A. Freeman, B. Delley, Phys. Rev. B **73**, 033203 (2006)

41. K. Raja, P.S. Ramesh, D. Geetha, Spectrochim. Acta A **120**, 19–24 (2014)

42. D. Theyvaraju, S. Muthukumaran, Physica E **74**, 93–100 (2015)

43. M. Ashokkumar, S. Muthukumaran, J. Lumin. **162**, 97–103 (2015)

44. M. Ahmad, E. Ahmed, Y. Zhang, N. Khalid, J. Xu, M. Ullah, Z. Hong, Curr. Appl. Phys. **13**, 697–704 (2013)

45. S. Singhal, J. Kaur, T. Namgyal, R. Sharma, Physica B **407**, 1223–1226 (2012)

46. S.D. Birajdar, P.P. Khirade, T.S. Saraf, R. Alange, K. Jadhav, J. Alloys Compd. **691**, 355–363 (2017)

47. J. Wang, G. Huang, X. Zhong, L. Sun, Y. Zhou, E. Liu, Appl. Phys. Lett. **88**, 252502 (2006)

48. P. Labhane, V. Huse, L. Patle, A. Chaudhari, G. Sonawane, J. Mater. Sci. Chem. Eng. **3**, 39 (2015)

49. U. Gahlaut, V. Kumar, R. Pandey, Y. Goswami, Optik **127**, 4292–4295 (2016)

50. A.S. Lanje, S.J. Sharma, R.S. Ningthoujam, J.-S. Ahn, R.B. Pode, Adv. Powder Technol. **24**, 331–335 (2013)

51. M. Iwamoto, in *Encyclopedia of Nanotechnology*, ed. by B. Bhushan. Maxwell–Wagner effect (Springer, New York, 2012), pp. 1276–1285

52. I. Gul, A. Abbasi, F. Amin, M. Anis-ur-Rehman, A. Maqsood, J. Magn. Magn. Mater. **311**, 494–499 (2007)

53. A. Ghosh, N. Kumari, A. Bhattacharjee, Pramana **84**, 621–635 (2015)

54. P. Capper, S. Kasap, A. Willoughby, *Zinc Oxide Materials for Electronic and Optoelectronic Device Applications* (Wiley, Hoboken, 2011)

55. A.J. Reddy, M. Kokila, H. Nagabhushana, R. Chakradhar, C. Shivakumara, J. Rao, B. Nagabhushana, J Alloys Compd. **509**, 5349–5355 (2011)

56. K. Noipa, S. Rujirawat, R. Yimnirun, V. Promarak, S. Maensiri, Appl. Phys. A **117**, 927–935 (2014)

57. C. Xia, C. Hu, Y. Tian, P. Chen, B. Wan, J. Xu, Solid State Sci. **13**, 388–393 (2011)

58. S. Riaz, S. Naseem, Y. Xu, J. Sol-Gel Sci. Technol. **59**, 584–590 (2011)

59. M. El-Hilo, A. Dakhel, A. Ali-Mohamed, J. Magn. Magn. Mater. **321**, 2279–2283 (2009)

60. R. Elilarassi, G. Chandrasekaran, J. Mater. Sci. Mater. Electron. **21**, 1168–1173 (2010)

61. D. Gao, Y. Xu, Z. Zhang, H. Gao, D. Xue, J. Appl. Phys. **105**, 063903 (2009)

62. N. Khare, M.J. Kappers, M. Wei, M.G. Blamire, J.L. MacManus-Driscoll, Adv. Mater. **18**, 1449–1452 (2006)

63. T.M. Hammad, J.K. Salem, R.G. Harrison, R. Hempelmann, N.K. Hejazy, J. Mater. Sci. Mater. Electron. **24**, 2846–2852 (2013)